

Controlling the Formation of Conductive Pathways in Memristive Devices

Robert Winkler, Alexander Zintler, Stefan Petzold, Eszter Piros, Nico Kaiser, Tobias Vogel, Déspina Nasiou, Keith P. McKenna, Leopoldo Molina-Luna,* and Lambert Alff*

Resistive random-access memories are promising candidates for novel computer architectures such as in-memory computing, multilevel data storage, and neuromorphics. Their working principle is based on electrically stimulated materials changes that allow access to two (digital), multiple (multilevel), or quasi-continuous (analog) resistive states. However, the stochastic nature of forming and switching the conductive pathway involves complex atomistic defect configurations resulting in considerable variability. This paper reveals that the intricate interplay of 0D and 2D defects can be engineered to achieve reproducible and controlled low-voltage formation of conducting filaments. The authors find that the orientation of grain boundaries in polycrystalline HfO_x is directly related to the required forming voltage of the conducting filaments, unravelling a neglected origin of variability. Based on the realistic atomic structure of grain boundaries obtained from ultra-high resolution imaging combined with first-principles calculations including local strain, this paper shows how oxygen vacancy segregation energies and the associated electronic states in the vicinity of the Fermi level govern the formation of conductive pathways in memristive devices. These findings are applicable to non-amorphous valence change filamentary type memristive device. The results demonstrate that a fundamental atomistic understanding of defect chemistry is pivotal to design memristors as key element of future electronics.

materials such as Hf-O or Ta-O , the conductive pathways consist of a local enrichment of oxygen vacancies.^[5-8] Pre-existing oxygen vacancies allow for low-voltage and thickness independent electroforming as only a reshuffle of vacancies is required.^[9-14] However, the oxygen vacancy distribution itself is still a random process associated with forming and operating voltage variability.^[15-17] Defect engineering to reduce the device variability has been investigated in several works using dislocations and nanocomposites.^[18-20] The introduction of threading grain boundaries (GBs) via GB engineering results in highly reproducible low-voltage electroforming.^[17] Here, we show that the complete materials picture is disclosed only when taking into account the intricate interplay between point-defects (oxygen vacancies) and 2D defect planes (grain boundaries). The specific atomic configurations of the grain boundaries including strain effects result in enhanced or suppressed attraction between both types of defects. As a consequence, the selection of the proper GB allows us to create a predefined region of increased oxygen vacancy concentration which is associated with electronic defect states close to


1. Introduction

A memristor is based on the controlled (digital or analog)^[1-4] change of the resistance of a conductive pathway. In complementary metal oxide semiconductor (CMOS) relevant

the Fermi level. These defect states, in turn, are the nuclei for the soft dielectric breakdown via formation of a defined conducting filament. This insight into the materials defect chemistry suggests new experimental methods of controlling the conducting

R. Winkler, S. Petzold, E. Piros, N. Kaiser, T. Vogel, L. Alff
Advanced Thin Film Technology Division
Institute of Materials Science
Technical University of Darmstadt
Alarich-Weiss-Straße 2, 64287 Darmstadt, Germany
E-mail: lambert.alf@tu-darmstadt.de

R. Winkler, A. Zintler, D. Nasiou, L. Molina-Luna
Advanced Electron Microscopy Division
Institute of Materials Science
Technical University of Darmstadt
Alarich-Weiss-Straße 2, 64287 Darmstadt, Germany
E-mail: leopoldo.molina-luna@aem.tu-darmstadt.de
K. P. McKenna
Department of Physics
The University of York
York YO10 5DD, UK

 The ORCID identification number(s) for the author(s) of this article can be found under <https://doi.org/10.1002/advs.202201806>

© 2022 The Authors. Advanced Science published by Wiley-VCH GmbH. This is an open access article under the terms of the Creative Commons Attribution License, which permits use, distribution and reproduction in any medium, provided the original work is properly cited.

DOI: 10.1002/advs.202201806

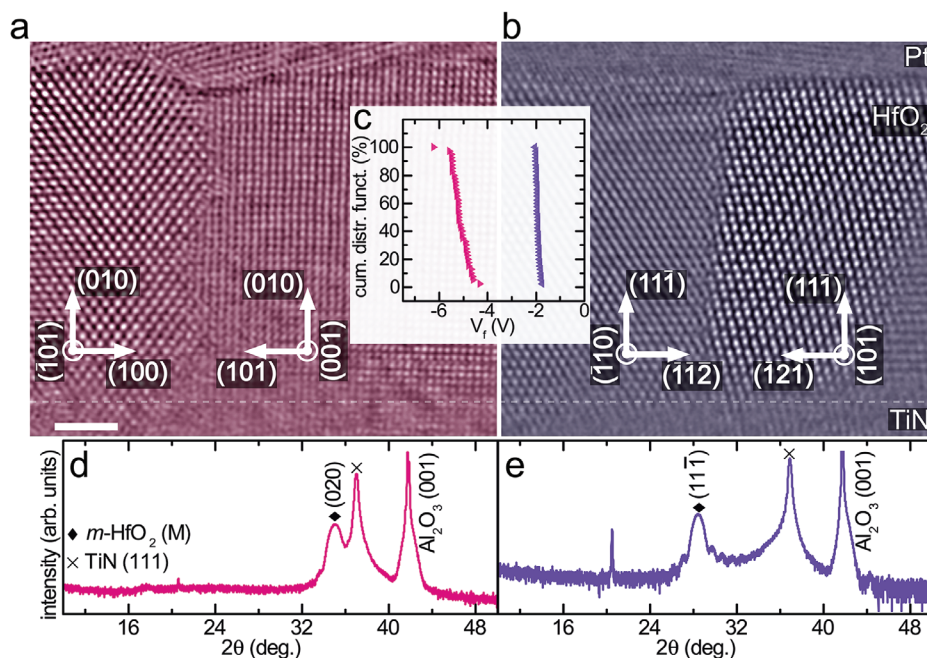


Figure 1. Cross-sectional high-angle annular dark-field (HAADF) scanning transmission electron microscopy (STEM) image of the metal-insulator-metal stack with a) (010) and b) (111) textured HfO₂. Scale bar is 2 nm. The TiN-HfO₂ interface is indicated by a faint dashed line. Images were filtered by an average background subtraction filter (ABSF), a Butterworth filter and a STEM crosshair filter to reduce image noise.^[25,26] Titanium nitride (TiN) and hafnium oxide (HfO₂) have been grown on (001) oriented Al₂O₃ by using RMBE. The X-ray diffraction (XRD) pattern reveals that a change in the growth temperature and rf-power for HfO₂ results in d) (111), (purple) and e) (020), (pink) when grown at 520 °C, 200 W and 460 °C, 280 W, respectively. c) Devices with (010) textured HfO₂ (pink) have an increased average forming voltage of $\bar{V}_f = -5.3$ V compared to devices with (111) HfO₂ having $\bar{V}_f = -1.9$ V as shown by the cumulative distribution function measured from 50 30 × 30 μm² devices. The purple XRD pattern, purple cumulative distribution of V_f and the purple colored high-resolution scanning transmission electron microscopy image is adapted from Petzold et al.^[17]

filament, and thus also serves as a valuable guideline for future memristor designs.^[21–34]

2. An Intriguing Observation: Electroforming Voltages Depend on Texture

The starting point of this investigation is the discovery of clearly distinct electroforming voltages in memristive model devices with different crystal orientation of the HfO₂ layer. The devices consist of a 50 nm TiN bottom electrode, followed by a 10 nm thin HfO₂ layer covered with Pt (100 nm) and gold (300 nm) grown on *c*-cut sapphire. When choosing the appropriate growth conditions either a (111) or (010) texture of the HfO₂ dielectric is achieved (Figure 1d,e and Figure S1, Supporting Information). We have verified the oxygen content by X-ray photoelectron spectroscopy revealing that the HfO₂ layers are homogeneously stoichiometric. Electroforming voltages were collected from 50 devices for each texture and reveal a clear correlation to the respective growth direction of HfO₂. For the (010) texture an average forming voltage of $\bar{V}_f = -5.3$ V was observed as compared to $\bar{V}_f = -1.9$ V for the (111) texture (see Figure 1c and Figure S2, Supporting Information). Both devices have a similar leakage current level at ±200 mV (see Figure S2a, Supporting Information). In addition to the very distinct quantitative voltage levels, the device-to-device variability is considerably reduced for the low voltage devices which are formed already at standard operation voltages (see Figure 1c).

2.1. Texture Defines Specific Grain Boundaries

Transmission electron microscopy revealed that the two types of textured HfO₂ layers are fully threaded by grain boundaries belonging to well-defined crystallographic equivalent sets of orientations (see Figure 1a,b). Such grain boundaries display characteristic periodic structure units that repeat themselves along the grain boundary plane (see purple and pink circles in Figures 2a and 3a). So far, grain boundaries have been discussed as a source of variability.^[27] Here we show that a smart use of grain boundaries may lead to the opposite, reduced, and more uniformly distributed forming voltage at negative bias. It is plausible to assume that grain boundaries in general provide a predefined pathway for filament formation.^[27] What is unexpected, however, is that there is a pronounced correlation of crystallographic directions and forming voltages, the latter ones being related to the electronic structure of the grain boundary. In the next step, therefore, we have used high-resolution imaging of atomic sites to model the real nanostructure of both grain boundary types using density functional theory (DFT). The DFT relaxed atomic structure for the (111) textured HfO₂ (see Figure 2b) is composed of one grain terminated by (112) and the other by (121). For (020) HfO₂ (Figure 3b), grains terminate at (100) and (101). The complete unit cells of these structures are shown in Figure S3, Supporting Information. The same periodically occurring structural units are again marked by purple and pink circles. The DFT calculation of the (112)|(121) grain boundary revealed two possible stable

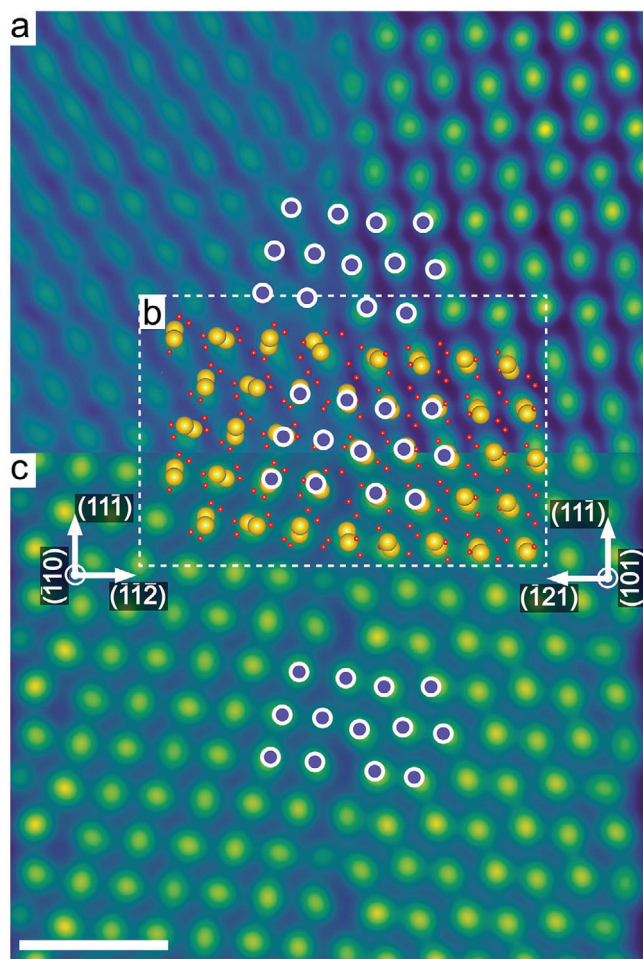


Figure 2. a) Cross-sectional high-angle annular dark-field (HAADF) scanning transmission electron microscopy (STEM) images of a grain boundary in (111) textured HfO_2 . The image was used as basis to simulate the b) DFT relaxed atomic structure model which were then used to simulate the HAADF-STEM image (c). Periodically occurring structural units at the grain boundaries are indicated by purple circles. Scale bar is 1 nm. Experimental HAADF-STEM images were filtered by an average background subtraction filter (ABSF) and a Butterworth filter to reduce image noise.^[25,26] All STEM images are colored with the GEM-16 LUT to improve visibility of atomic columns.

structures differing only by a rigid translation of one grain with respect to each other (Figure S4, Supporting Information). To validate if these models replicate the real complex atomic structures, multislice-based electron microscopy image simulations were performed (Figures 2c and 3c). The results match with high accuracy the atomically resolved HAADF-STEM data. This result shows that imaging of defect processes at grain boundaries can be obtained not only on well-defined bicrystals,^[28,29] but can be extended to realistic CMOS materials.

It is important to note that for (111) textured HfO_2 , construction of the $(\overline{112})|(\overline{1}21)$ GB was only possible by applying significant strain parallel to the grain boundary. In contrast, the construction of the (100)|(101) grain boundary for (020) HfO_2 requires no strain most likely due to the semi-coherent nature of this grain boundary.^[30] Strain effects by lattice mismatch or

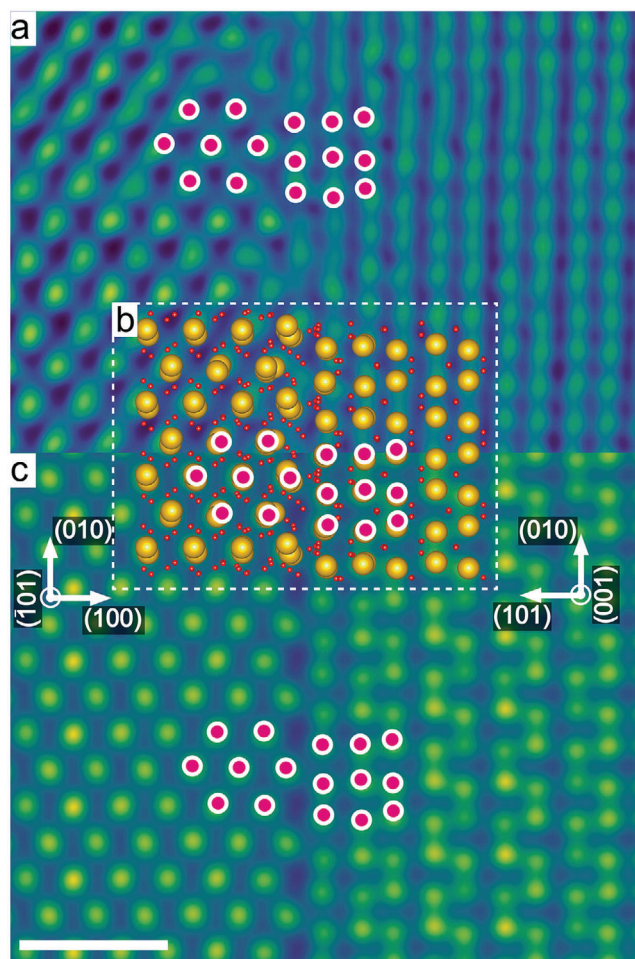


Figure 3. a) Cross-sectional high-angle annular dark-field (HAADF) scanning transmission electron microscopy (STEM) images of a grain boundary in (020) textured HfO_2 . The image was used as basis to simulate the b) DFT relaxed atomic structure model which was then used to simulate the HAADF-STEM image (c). Periodically occurring structural units at the grain boundaries are indicated by pink circles. Scale bar is 1 nm. Experimental HAADF-STEM images were filtered by an average background subtraction filter (ABSF) and a Butterworth filter to reduce image noise.^[25,26] All STEM images are colored with the GEM-16 LUT to improve visibility of atomic columns.

dopants are being routinely used in semiconductor technology to modify electronic properties and transistor performance.^[31] Here we show that texture transfer induced strain in coherent grain boundaries have a strong effect on electronic properties in memristive devices.

2.2. Grain Boundary Influence on Oxygen Segregation Energies and Electronic Structure

Having properly modelled the grain boundary defect nanostructures of realistic memristive model devices gives us the possibility to investigate neutral oxygen vacancy (V_{O}) interactions with GBs by first principles calculations. Note that we are not using a model grain boundary of higher symmetric (cubic) HfO_2 but are taking the real atomic positions of the grain boundary within

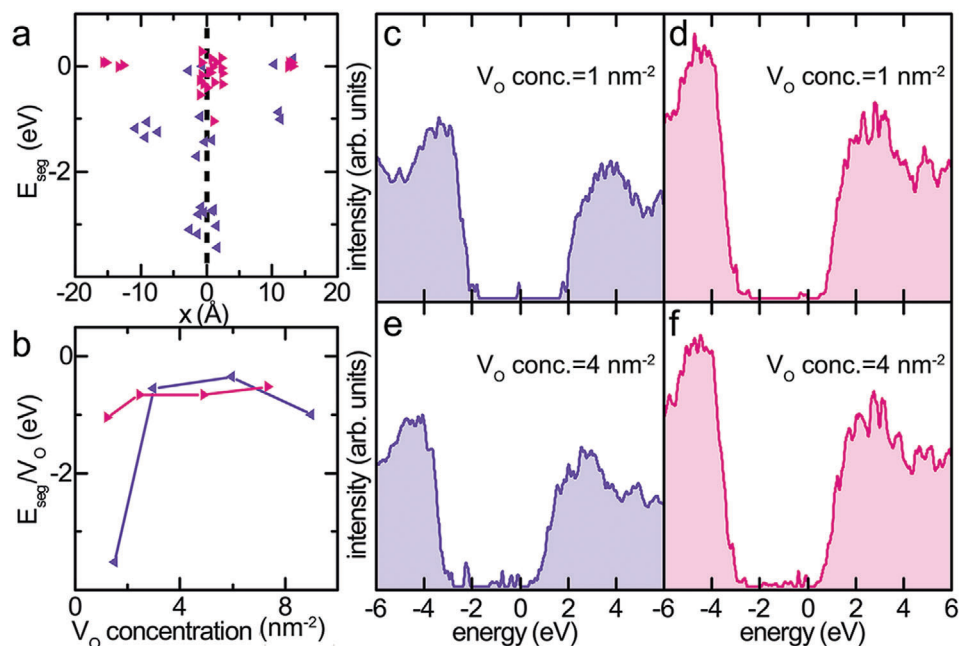


Figure 4. Oxygen vacancy segregation energies were calculated from the DFT relaxed atomic structure models as a function of a) distance from the grain boundary (marked by dotted line) and b) oxygen vacancy concentration for (111), (purple) and (020), and (pink) textured HfO₂. The density of states (DOS) at grain boundaries for c,e) (111) and d,f) (020) HfO₂ were calculated using the projector augmented wave (PAW) method and are shown as a function of oxygen vacancy concentration (V_O conc.).

the monoclinic phase. The variation of segregation energy E_{seg} in the vicinity of the GBs (Figure 4a) shows that oxygen vacancy segregation is more favorable at the $(\bar{1}1\bar{2})|(\bar{1}21)$ GB (purple) than at the (100)|(101) GB (pink). However, as the concentration of vacancies increases beyond 2 nm^{-2} the average segregation energy per vacancy (E_{seg}/V_O) for the two GBs becomes comparable (Figure 4b). The electronic properties investigated by the density of states (DOS) projected onto the GB regions (Figure 4c) as a function of V_O concentration reveal a larger band gap for the $(\bar{1}1\bar{2})|(\bar{1}21)$ GB (purple) than the (100)|(101) GB (pink). The magnitude of the band gaps is comparable to previous reports^[32,33] and in the presence of V_O the bandgaps are significantly smaller as compared to bulk $m\text{-HfO}_2$.^[34,35] For low V_O concentration (below 2 nm^{-2}) the DOS of both GBs show a deep and narrow gap state associated with the vacancies.^[34]

For the $(\bar{1}1\bar{2})|(\bar{1}21)$ GB, the gap state is positioned mid-gap, while for the (100)|(101) GB the gap state is positioned closer to the conduction band. With increase in V_O concentration the DOS shows the formation of a conductive sub-band as suggested in literature.^[33,35] DOS for V_O concentration equal to 0, 2, and 6 nm^{-2} are shown in Figure S5, Supporting Information.

The electronic properties investigated by the DOS from the DFT relaxed structures of the $(\bar{1}1\bar{2})|(\bar{1}21)$ GB and the (100)|(101) GB were comparable and the introduction of oxygen vacancies resulted in a similar change of the intermediate bandgap states of the DOS. The formed conductive sub-band for V_O concentration above 2 nm^{-2} is a percolation path for the current and deteriorates the insulating properties of HfO₂. The oxygen vacancy concentration can be driven even to a state where the insulator transitions to a semiconducting or even metallic state.^[35] The presence

of preexisting oxygen vacancies is known to reduce the required forming voltages for a conductive filament in HfO_{2-x}.^[12] For the here discussed samples, the stoichiometry of the HfO₂ matrix is close to the ideal 1:2. It can, therefore, be excluded that any anisotropy in oxygen vacancy distribution inside the nanocrystals is the reason for the difference in forming voltages. Therefore, the V_O concentration below 2 nm^{-2} is representative for a pristine non-formed resistive switching device, which is insulating. Our results show that at low vacancy concentrations the V_O segregation energy in $(\bar{1}1\bar{2})|(\bar{1}21)$ GBs (in comparison to the (100)|(101) GBs) are more negative. The $(\bar{1}1\bar{2})|(\bar{1}21)$ GB therefore acts as a sink for oxygen vacancies, thereby, driving the surrounding matrix closer to perfect stoichiometry by the depletion of vacancies, while the grain boundary plane itself is enriched in vacancies. As a consequence, this type of grain boundary is the perfect percolation path for electron transport initiating the formation of a conducting filament.

Due to the monoclinic structure of the HfO₂ thin films, imaging a grain boundary with both grains being atomically resolved was highly challenging. Moreover, finding a high resolved GB did not guarantee that the construction of a DFT relaxed supercell was possible due to the non-commensurate nature of adjacent monoclinic grains. Therefore, only one GB of each HfO₂ texture is shown. However, the textured growth of the (111) and (020) HfO₂ thin films results in six allowed in-plane directions each (Figure S6a,b, Supporting Information) limiting the possible orientations and resultant GB types. According to Figure S6c,d, Supporting Information, the majority of GBs in (020) textured HfO₂ are therefore composed of grains terminated by low-index orientations (e.g., (100)), contrary to GBs in (111) HfO₂ which have

high-indexed terminated grains. Construction of the GB with high-indexed terminated grains ($(\bar{1}12)|(\bar{1}21)$ GB) required application of strain. In the near future, we plan to probe local stress fields of GBs with high- and low-indexed terminating grains to investigate the effect on local ionic mobility.^[36–41]

3. Conclusion

Our combined experimental and ab initio study reveals that an intricate interplay of defects with different dimensionality plays the key role in predefining the formation path of the conducting filament. The controlled induction of a specific grain boundary type by texture transfer is a promising way to overcome present limitations set by the variability of forming voltages and is likely to be favorable for improved device endurance and cycle stability. For the sake of this study we have used MBE growth parameters outside the CMOS temperature budget. However, the favorable combination of a (111) oriented TiN electrode with a (11-1) oriented HfO₂ functional layer can also be achieved with industrial relevant methods such as atomic layer deposition. The here suggested method of grain boundary and defect engineering is scalable well below 10 nm as the grain size is comparable to the thickness of the dielectric layer.

4. Experimental Section

Sample Preparation: Reactive molecular beam epitaxy (RMBE) was used to grow TiN on *c*-cut sapphire followed by in situ growing HfO₂ in a custom designed ultra-high vacuum chamber (base pressure $\approx 10^{-9}$ mbar).^[42] For the TiN layers, the substrate was heated to 800 °C. Ti from Lesker (4.5 N purity) was evaporated at a rate of 0.3 Å s⁻¹ with in situ nitridation by using a radio frequency (rf)-source with an rf-power of 350 W and a flow of 0.6 sccm nitrogen (5 N purity). Growth of hafnia layers with defined textures were achieved by using distinct temperatures and rf-powers. Hf from MaTeck (3 N purity) was evaporated at a rate of 0.7 Å s⁻¹ and in situ oxidized by a rf-source with a flow of 1 sccm oxygen (5 N purity). For the $(1\bar{1}\bar{1})$ textured hafnia, the rf-source was operated at 200 W and the substrate was heated to 520 °C. The (020) textured hafnia was grown at a substrate temperature of 460 °C with the rf-source operating at 280 W. The film thickness and surface crystallinity were in situ monitored by using quartz crystal microbalance (QCM) and reflection high energy electron diffraction (RHEED), respectively. To complement the metal–insulator–metal (MIM) structure, first a standard lithography step was carried out to pattern the surface followed by sputtering 100 nm Pt and 300 nm Au with a Quorum sputter cutter. The lift-off process resulted in $30 \times 30 \mu\text{m}^2$ MIM devices.

X-Ray Measurements: Before completing the MIM structure, texture quality of the reactive molecular beam epitaxy (RMBE)-grown TiN and HfO₂ thin films were examined with X-ray diffractometry (XRD). A Rigaku SmartLab diffractometer were used in parallel beam geometry with a copper K_α X-ray source.

Electroforming: Initialization of resistive switching for a device under test (DUT) was achieved by a DC-negative voltage sweep using a Keithley 4200 semiconductor characterization system (SCS). The top electrode of the device under test (DUT) was biased while electrically grounding the bottom electrode. To prevent a hard dielectric breakdown during electroforming, the internal current compliance (CC) of the semiconductor characterization system (SCS) was limited to 10 and 100 μA.

Electron Microscopy: From the MIM devices, TEM lamellae were prepared by using in situ lift-out focused ion beam (FIB) microscopy (JEOL JIB-4600F). Aberration corrected STEM images were acquired with a convergence angle of 36 mrad by using a field-emission (S)TEM (JEOL ARM-200F) at an acceleration voltage of 200 kV. Detection angles of the HAADF

detector ranged from 90 to 370 mrad. Growth direction and zone axis of the HfO₂ thin films were identified by using the diffractGUI of CrysTBox developed by Klinger and Jäger^[43] with the FFTs of individual grains and a reference structure from Christensen and An^[44] as the material input.

Density Functional Theory Methodology: Calculations of the structure and electronic properties of *m*-HfO₂ GBs were performed using the projector augmented wave (PAW) method as implemented in the Vienna Ab-initio Simulation Package (VASP).^[45,46] The approach was the same as that described in the authors' previous paper which focused on a single GB type observed in $(1\bar{1}\bar{1})$ textured films.^[17] Here a second GB type observed in (020) textured films was also considered as well as V_O segregation to both GB models was considered in order to provide insight into the origin of the difference in V_F. The generalized gradient approximation of Perdew, Burke, and Ernzerhof (PBE)^[47] and standard Hf and soft oxygen projector augmented wave (PAW) potentials was employed. Using a 400 eV plane wave cut-off and a Monkhorst–Pack k-point grid of $11 \times 11 \times 11$ lattice constants for bulk *m*-HfO₂ within 0.5% of experimental values were obtained.

The GB in the $(1\bar{1}\bar{1})$ textured films could be formed by joining a $(\bar{1}\bar{1}\bar{2})$ terminated *m*-HfO₂ grain to a $(\bar{1}21)$ terminated grain. To make a commensurate supercell in this case one must apply strain to both grains parallel to the interface (<10%). The grain boundary in the (020) textured films could be formed by joining a (100) terminated *m*-HfO₂ grain to a (101) terminated grain. In this case, it was possible to form a commensurate supercell with very little strain (<0.1%). For both GB models, a vacuum gap of 10 Å was included to separate the two free surfaces in the periodic supercell such that only one GB interface was present. This was necessary in this case as the low symmetry of the GB makes it impossible to construct two equivalent GB interfaces in the supercell as is usually possible for higher symmetry GBs.^[48–51] To determine the most stable configuration, a gamma-surface scan of GB translation states was carried out (in steps of ≈ 1 Å in both directions parallel to the grain boundary).

To assess the tendency of V_O to segregate to the GBs, vacancy formation energies for all inequivalent oxygen sites in the region between the centers of each grain were calculated. The formation energy was computed relative to half the energy of an oxygen molecule. For the (020) textured GB (which had negligible in-plane strain applied), the formation energies in the bulk of each grain were very similar and in good agreement with previous calculations of V_O in bulk *m*-HfO₂ (6.57 eV for three-coordinated sites and 6.64 eV for four-coordinated sites). Because the $(1\bar{1}\bar{1})$ textured grain boundary had significant strain applied, the absolute formation energies in the bulk of each grain were modified (≈ 1.2 eV lower in energy). To allow comparison and assess general trends in defect segregation, a segregation energy (E_{seg}) is defined relative to the bulk formation energy in each GB model. In both models, vacancy segregation was favorable both in the dilute limit and, as the concentration of vacancies segregated to the grain boundaries, was increased. To assess the effect this has on electronic properties, the electronic DOS both for the pristine stoichiometric GB and the GB with increasing concentrations of V_O were computed.

Multislice Simulations: To correlate experimental high-resolution data to the developed supercells from density functional calculations, STEM images were simulated with the software Dr. Probe^[52] using the multislice method.^[53] Within the software, the microscope parameters were set to an acceleration voltage of 200 kV, a convergence angle of 25 mrad, a source size of 0.08 nm, and a HAADF detection range of 90 to 370 mrad with all aberrations set to zero. Cell sizes for equidistant slice creation along *z* with applied Debye–Waller factors for the $(\bar{1}\bar{1}\bar{2})|(\bar{1}21)$ and the (100)|(101) GB were $10.49 \times 1.90 \times 14.03$ nm, $4800 \text{ pixel} \times 864 \text{ pixel} \times 80$ slices, $19 \ 200$ atoms and $11.77 \times 1.03 \times 15.87$ nm, $5400 \text{ pixel} \times 480 \text{ pixel} \times 180$ slices, $13 \ 920$ atoms ($x \times y \times z$), respectively. Centered calculation windows were set to 5.24×0.95 nm, 524×95 pixels and 5.89×0.52 nm, 589×52 pixels ($x \times y$) with a sampling of 0.01 nm/pix for the $(\bar{1}\bar{1}\bar{2})|(\bar{1}21)$ and the (100)|(101) GB, respectively. Computational time for a “Scan image” type with a thickness of ≈ 10 nm (56 and 113 slices, respectively) took ≈ 2 h 30 min and ≈ 2 h for the $(\bar{1}\bar{1}\bar{2})|(\bar{1}21)$ and the (100)|(101) GB, respectively, using 30 threads of an AMD Ryzen 9 3950X CPU overclocked to 4.15 GHz

assisted by a GeForce RTX 3070 GPU (128 GB 2666 MHz RAM and 500 GB Samsung SSD 970 EVO Plus).

Supporting Information

Supporting Information is available from the Wiley Online Library or from the author.

Acknowledgements

This work was supported by the European Research Council (ERC) "Horizon 2020" Program under Grant No. 805359-FOXON and Grant No. 957521-STARE and the Deutsche Forschungsgemeinschaft (DFG) under projects MO 3010/3-1 and AL 560/21-1. The work was supported by the framework of the WAKeMeUP and StorAlge project which received funding from the Electronic Components and Systems for European Leadership Joint Undertaking in collaboration with the European Union's H2020 Framework Programme (H2020/2014-2020) and National Authorities, under grant agreement No. 783176 and No. 101007321, respectively. Funding by the Federal Ministry of Education and Research (BMBF) under contract 16ESE0298 and 16MEE0154 are gratefully acknowledged. E.P. acknowledges funding from the Deutscher Akademischer Austauschdienst (DAAD). K.P.M. acknowledges support from EPSRC (EP/P023843/1) and access to the Viking Cluster, which is a high-performance computing facility provided by the University of York. All data relating to the density functional theory calculations are available by request from the University of York Research database.

Open Access funding enabled and organized by Projekt DEAL.

Conflict of Interest

The authors declare no conflict of interest.

Author Contributions

L.A. and S.P. started and suggested the study. L.A., L.M.-L. supervised and steered the ongoing project. R.W., N.K., S.P., and T.V. were responsible for sample synthesis and electrical characterization. R.W., D.N., and A.Z. performed the TEM measurements and multislice simulations. K.P.M. performed the DFT calculations. L.A., R.W., L.M.-L., E.P., S.P., and A.Z. wrote the manuscript. All authors discussed the results and provided constructive comments on the manuscript.

Data Availability Statement

The data that support the findings of this study are available from the corresponding author upon reasonable request.

Keywords

first principle calculation, grain boundary atomic structures, hafnium oxide, resistive switching memory, scanning transmission electron microscopy

Received: March 28, 2022

Revised: June 21, 2022

Published online: September 8, 2022

[1] Z. Wang, H. Wu, G. W. Burr, C. S. Hwang, K. L. Wang, Q. Xia, J. J. Yang, *Nat. Rev. Mater.* **2020**, *5*, 173.

- [2] D. Ielmini, S. Ambrogio, *Nanotechnology* **2019**, *31*, 092001.
- [3] International Roadmap for Devices and Systems (IRDSTM) 2020 Edition - IEEE IRDSTM, <https://irds.ieee.org/editions/2020> (accessed: December 2021).
- [4] D. Marković, A. Mizrahi, D. Querlioz, J. Grollier, *Nat. Rev. Phys.* **2020**, *2*, 499.
- [5] D. Ielmini, R. Waser, *Resistive Switching: From Fundamentals of Nanoionic Redox Processes to Memristive Device Applications*, Wiley-VCH, Weinheim **2015**.
- [6] B. Govoreanu, G. S. Kar, Y. Y. Chen, V. Paraschiv, S. Kubicek, A. Fantini, I. P. Radu, L. Goux, S. Clima, R. Degraeve, N. Jossart, O. Richard, T. Vandeweyer, K. Seo, P. Hendrickx, G. Pourtois, H. Bender, L. Altissime, D. J. Wouters, J. A. Kittl, M. Jurczak, 2011 Int. Electron Devices Meet, IEEE, Piscataway, NJ **2011**, pp. 31.6.1-31.6.4.
- [7] Y. Hayakawa, A. Himeno, R. Yasuhara, W. Boullart, E. Vecchio, T. Vandeweyer, T. Witters, D. Crotti, M. Jurczak, S. Fujii, S. Ito, Y. Kawashima, Y. Ikeda, A. Kawahara, K. Kawai, Z. Wei, S. Muraoka, K. Shimakawa, T. Mikawa, S. Yoneda, 2015 Symp. VLSI Technol. (VLSI Technol.) IEEE, Piscataway, NJ **2015**, pp. T14-T15.
- [8] Z. Wei, T. Takagi, Y. Kanzawa, Y. Katoh, T. Ninomiya, K. Kawai, S. Muraoka, S. Mitani, K. Katayama, S. Fujii, R. Miyayama, Y. Kawashima, T. Mikawa, K. Shimakawa, K. Aono, 2011 Int. Electron Devices Meet IEEE, Piscataway, NJ **2011**, pp. 31.4.1-31.4.4.
- [9] S. U. Sharath, T. Bertaud, J. Kurian, E. Hildebrandt, C. Walczyk, P. Calka, P. Zaumseil, M. Sowinska, D. Walczyk, A. Gloskovskii, T. Schroeder, L. Alff, *Appl. Phys. Lett.* **2014**, *104*, 063502.
- [10] S. U. Sharath, J. Kurian, P. Komissinskiy, E. Hildebrandt, T. Bertaud, C. Walczyk, P. Calka, T. Schroeder, L. Alff, *Appl. Phys. Lett.* **2014**, *105*, 073505.
- [11] S. U. Sharath, M. J. Joseph, S. Vogel, E. Hildebrandt, P. Komissinskiy, J. Kurian, T. Schroeder, L. Alff, *Appl. Phys. Lett.* **2016**, *109*, 173503.
- [12] S. U. Sharath, S. Vogel, L. Molina-Luna, E. Hildebrandt, C. Wenger, J. Kurian, M. Duerrschabel, T. Niemann, G. Niu, P. Calka, M. Lehmann, H.-J. Kleebe, T. Schroeder, L. Alff, *Adv. Funct. Mater.* **2017**, *27*, 1700432.
- [13] S. Petzold, E. Miranda, S. Sharath, J. Muñoz-Gorritz, T. Vogel, E. Piros, N. Kaiser, R. Eilhardt, A. Zintler, L. Molina-Luna, *J. Appl. Phys.* **2019**, *125*, 234503.
- [14] S. Petzold, E. Piros, R. Eilhardt, A. Zintler, T. Vogel, N. Kaiser, A. Radetinac, P. Komissinskiy, E. Jalaguier, E. Nolot, C. Charpin-Nicolle, C. Wenger, L. Molina-Luna, E. Miranda, L. Alff, *Adv. Electron. Mater.* **2020**, *6*, 2000439.
- [15] C. Baeumer, R. Valenta, C. Schmitz, A. Locatelli, T. O. Menteş, S. P. Rogers, A. Sala, N. Raab, S. Nemsak, M. Shim, C. M. Schneider, S. Menzel, R. Waser, R. Dittmann, *ACS Nano* **2017**, *11*, 6921.
- [16] S. Ambrogio, S. Balatti, A. Cubeta, A. Calderoni, N. Ramaswamy, D. Ielmini, *IEEE Trans. Electron Devices* **2014**, *61*, 2920.
- [17] S. Petzold, A. Zintler, R. Eilhardt, E. Piros, N. Kaiser, S. U. Sharath, T. Vogel, M. Major, K. P. McKenna, L. Molina-Luna, *Adv. Electron. Mater.* **2019**, *5*, 1900484.
- [18] W. Banerjee, Q. Liu, H. Hwang, *J. Appl. Phys.* **2020**, *127*, 051101.
- [19] S. Choi, S. H. Tan, Z. Li, Y. Kim, C. Choi, P.-Y. Chen, H. Yeon, S. Yu, J. Kim, *Nat. Mater.* **2018**, *17*, 335.
- [20] M. N. Martyshev, A. V. Emelyanov, V. A. Demin, K. E. Nikiryu, A. A. Minnekhanov, S. N. Nikolaev, A. N. Taldenkov, A. V. Ovcharov, M. Y. Presnyakov, A. V. Sitnikov, A. L. Vasiliev, P. A. Forsh, A. B. Granovsky, P. K. Kashkarov, M. V. Kovalchuk, V. V. Rylov, *Phys. Rev. Appl.* **2020**, *14*, 034016.
- [21] A. Sebastian, M. L. Gallo, R. Khaddam-Aljameh, E. Eleftheriou, *Nat. Nanotechnol.* **2020**, *15*, 529.
- [22] K. Sun, J. Chen, X. Yan, *Adv. Funct. Mater.* **2021**, *31*, 2006773.
- [23] D. Ielmini, H.-S. P. Wong, *Nat. Electron.* **2018**, *1*, 333.
- [24] M. A. Zidan, Y. Jeong, J. Lee, B. Chen, S. Huang, M. J. Kushner, W. D. Lu, *Nat. Electron.* **2018**, *1*, 411.

- [25] A. Rosenauer, S. Kaiser, T. Reisinger, J. Zweck, W. Gebhardt, D. Gerthsen, *Optik* **1996**, 102, 63.
- [26] R. Kilaas, *J. Microsc.* **1998**, 190, 45.
- [27] M. Lanza, *Materials* **2014**, 7, 2155.
- [28] J. Wei, B. Feng, R. Ishikawa, T. Yokoi, K. Matsunaga, N. Shibata, Y. Ikuhara, *Nat. Mater.* **2021**, 20, 951.
- [29] E. Tochiga, Y. Kezuka, A. Nakamura, N. Shibata, Y. Ikuhara, *Nano Lett.* **2017**, 17, 2908.
- [30] G. B. Olson, M. Cohen, *Acta Metall.* **1979**, 27, 1907.
- [31] Y. Sun, S. E. Thompson, T. Nishida, *J. Appl. Phys.* **2007**, 101, 104503.
- [32] K.-H. Xue, P. Blaise, L. R. C. Fonseca, G. Molas, E. Vianello, B. Traoré, B. De Salvo, G. Ghibaudo, Y. Nishi, *Appl. Phys. Lett.* **2013**, 102, 201908.
- [33] G. Bersuker, J. Yum, V. Iglesias, M. Porti, M. Nafria, K. McKenna, A. Shluger, P. Kirsch, R. Jammy, 2010 Proc. Eur. Solid State Device Res. Conf. **2010**, pp. 333-336.
- [34] K. H. Xue, B. Traore, P. Blaise, L. R. C. Fonseca, E. Vianello, G. Molas, B. D. Salvo, G. Ghibaudo, B. Magyari-Kope, Y. Nishi, *IEEE Trans. Electron Devices* **2014**, 61, 1394.
- [35] E. Hildebrandt, J. Kurian, M. M. Müller, T. Schroeder, H.-J. Kleebe, L. Alff, *Appl. Phys. Lett.* **2011**, 99, 112902.
- [36] J. A. Kilner, *Nat. Mater.* **2008**, 7, 838.
- [37] R. Pornprasertsuk, P. Ramanarayanan, C. B. Musgrave, F. B. Prinz, *J. Appl. Phys.* **2005**, 98, 103513.
- [38] A. Kushima, B. Yildiz, *J. Mater. Chem.* **2010**, 20, 4809.
- [39] B. Yildiz, *MRS Bull.* **2014**, 39, 147.
- [40] C. Jiang, N. Swaminathan, J. Deng, D. Morgan, I. Szlufarska, *Mater. Res. Lett.* **2014**, 2, 100.
- [41] N. Chen, L.-L. Niu, Y. Zhang, X. Shu, H.-B. Zhou, S. Jin, G. Ran, G.-H. Lu, F. Gao, *Sci. Rep.* **2016**, 6, 36955.
- [42] A. Buckow, R. Retzlaff, J. Kurian, L. Alff, *Supercond. Sci. Technol.* **2012**, 26, 015014.
- [43] M. Klinger, A. Jäger, *J. Appl. Crystallogr.* **2015**, 48, 2012.
- [44] R. Ruh, P. W. R. Corfield, *J. Am. Ceram. Soc.* **1970**, 53, 126.
- [45] G. Kresse, J. Hafner, *Phys. Rev. B* **1993**, 47, 558.
- [46] G. Kresse, J. Hafner, *Phys. Rev. B* **1994**, 49, 14251.
- [47] J. P. Perdew, K. Burke, M. Ernzerhof, *Phys. Rev. Lett.* **1996**, 77, 3865.
- [48] J. J. Bean, M. Saito, S. Fukami, H. Sato, S. Ikeda, H. Ohno, Y. Ikuhara, K. P. McKenna, *Sci. Rep.* **2017**, 7, srep45594.
- [49] K. P. McKenna, *ACS Energy Lett.* **2018**, 3, 2663.
- [50] C. J. Tong, K. P. McKenna, *J. Phys. Chem. C* **2019**, 123, 23882.
- [51] J. A. Quirk, V. K. Lazarov, K. P. McKenna, *Adv. Theory Simul.* **2019**, 2, 1900157.
- [52] J. Barthel, *Ultramicroscopy* **2018**, 193, 1.
- [53] J. M. Cowley, A. F. Moodie, *Acta Crystallogr.* **1957**, 10, 609.